

Citation for published version:

Jolly, P, Rainbow, J, Regoutz, A, Estrela, P & Moschou, D 2019, 'A PNA-based Lab-on-PCB diagnostic platform for rapid and high sensitivity DNA quantification', *Biosensors and Bioelectronics*, vol. 123, pp. 244-250.
<https://doi.org/10.1016/j.bios.2018.09.006>

DOI:

[10.1016/j.bios.2018.09.006](https://doi.org/10.1016/j.bios.2018.09.006)

Publication date:

2019

Document Version

Peer reviewed version

[Link to publication](#)

Publisher Rights

CC BY-NC-ND

University of Bath

Alternative formats

If you require this document in an alternative format, please contact:
openaccess@bath.ac.uk

General rights

Copyright and moral rights for the publications made accessible in the public portal are retained by the authors and/or other copyright owners and it is a condition of accessing publications that users recognise and abide by the legal requirements associated with these rights.

Take down policy

If you believe that this document breaches copyright please contact us providing details, and we will remove access to the work immediately and investigate your claim.

A PNA-based Lab-on-PCB diagnostic platform for rapid and high sensitivity

DNA quantification

Pawan Jolly^{*1, 2, †}, Joshua Rainbow¹, Anna Regoutz³, Pedro Estrela¹, Despina Moschou^{*1, 2}

¹ Centre for Biosensors, Bioelectronics and Biodevices (C3Bio) and Department of Electronic and Electrical Engineering, University of Bath, Bath, BA2 7AY, UK.

² DxOnBoard Ltd, Carpenter House, Broad Quay, Bath, BA1 1UD, UK.

³ Department of Materials, Imperial College London, London, SW7 2AZ, UK.

[†] Current address: Wyss Institute for Biologically Inspired Engineering at Harvard University, Boston, 02115, MA, USA.

**Corresponding Authors:* Phone: +44 (0) 1225383245, Email: Pawan.Jolly@wyss.harvard.edu (Pawan Jolly), D.Moschou@bath.ac.uk (Despina Moschou)

Abstract

We report the development of a Lab-on-PCB DNA diagnostic platform, exploiting peptide nucleic acid (PNA) sequences as probes. The study demonstrates the optimization and characterization of two commercial PCB manufacturing gold electroplating processes for biosensing applications. Using an optimized ratio of PNA with a spacer molecule (MCH), the lowest limit of detection (LoD) to date for PCB-based DNA biosensors of 57 fM is reported. The study also showcases a fully integrated Lab-on-PCB microsystem designed for rapid detection, which employs PCB-integrated sample delivery, achieving DNA quantification in the 0.1-100 pM range for 5 μ L samples analyzed within 5 minutes under continuous flow. The demonstrated biosensor proves the capability of PCB-based DNA biosensors for high sensitivity and paves the way for their integration in Lab-on-PCB DNA diagnostic microsystems.

Keywords: PNA, PCB, DNA, nucleic acid, impedimetric, biosensor

1. Introduction

Lab-on-Chip (LoC) devices combining cost effectiveness with high performance, are a key technological enabler for future Point-of-Care (PoC) diagnostic devices. Lab on printed circuit board (Lab-on-PCB) is re-emerging as a promising mass-manufacturing technology for seamlessly integrated microsystems (Chin et al., 2012; Jung et al., 2015). In principle, PoC tests should meet the ASSURED criteria: affordability, sensitivity, specificity, user friendly, rapid analysis, equipment-free operation, and capability to be delivered to those who need it (Yetisen et al., 2013). To take up the challenge, LoC technology allows sensitive and specific analysis via integrated sensors, rapid analysis due to system miniaturization, user-friendliness by implementing sample-in-answer-out microsystems, affordability by minimizing reagent volumes and fabricating cost-effective devices and even equipment-free operation through implementing fully autonomous systems (e.g. integrating sample handling and sensor read-out). Several LoC approaches are being explored, in an effort to define a cost-effective and standardized fabrication technology for integrated devices fully meeting the ASSURED criteria in real-life clinical applications.

Whilst first suggested in the late 1990s (van den Berg & Lammerink, 1998), the Lab-on-PCB approach has seen increasing interest for cost-effective integrated LoCs over the past decade (Aracil et al., 2015). Its main advantage over alternative technologies (e.g. Si, glass, polymer, or paper) is the exploitation of a long-standing, established and standardized industrial infrastructure (Mahato et al., 2017). This promises truly low-cost, standardized manufacturing for LoC devices integrating sample pre-treatment microfluidics, sensitive and specific electrochemical biosensors, and electronics, through economy of scale mass manufacturing (Moschou & Tserepi, 2017). Aiming to fully exploit these advantages,

highly promising Lab-on-PCB microsystems and components have been demonstrated (Fu et al., 2017; Hintermüller et al., 2017; Sanchez et al., 2016), with the concurrent goal to adapt Lab-on-PCB fabrication to commercially available manufacturing processes (Moschou et al., 2016; Moschou & Tserepi, 2017).

This study aims to develop a fully integrated Lab-on PCB device by utilizing peptide nucleic acid (PNA) as a probe for novel genetic analysis. Even today, genetic analysis using DNA, RNA, miRNA and cRNA microsystems still remains the key objective for various clinical applications (e.g. infectious disease and cancer diagnostics). PNA molecules are synthetic analogues of DNA consisting of a backbone of repeating units of N-(2-aminoethyl) glycine linked via an amide bond (Cai et al., 2014; Jolly et al., 2016). In PNA, the four naturally occurring nucleobases, namely adenine, cytosine, guanine, and thymine, are connected to the central amine of the peptide backbone via a methylene bridge and a carbonyl group. Such a modification changes the negative charge of the DNA sugar-phosphate backbone to a neutral charge of the peptide-like backbone. As a consequence, the PNA/DNA duplex demonstrates higher binding efficiency, thermal stability, and independence of the PNA/DNA duplex stability on the ionic strength of the solution in which hybridization is performed (Hyrup & Nielsen, 1996). A significant amount of the literature on the electrochemical detection of DNA uses self-assembled monolayers (SAM) with DNA or PNA probes on macroscale electrodes; although this approach is a critical first step in realizing practical, miniaturized biosensing microsystems, employing the developed assays repeatably and reliably in commercially upscalable microsystems surfaces is not straightforward and is a topic in which the scientific community has little insight, hindering the real-life deployment of the numerous electrochemical biosensor assays presented currently (Bizzotto D et al, 2018).

In this paper we address systematically this issue in SAM/PNA/DNA systems, taking both our and the biosensor community's work to the next step: understanding how high-performance assays can be employed in commercially fabricated sensing microelectrodes. We also highlight and analyze by thorough surface analysis the critical importance of electroplating techniques and their resulting surface characteristics (surface roughness and chemical purity) in achieving sensitivities comparable to the more ideal macroelectrode surfaces. This study results in the highest-sensitivity PCB-implemented DNA EIS sensors ever reported (Limit of Detection of 57 fM). We also seamlessly integrate the characterized biosensors with reagent delivery microfluidics in a Lab-on-PCB microsystem, and compare their performance under continuous flow, following the operation of a real-life diagnostic microsystem. We demonstrate that employing only 5 μ L of sample, it is possible to achieve sensitive DNA quantification within only 5 minutes. The effects of continuous liquid flow in several biosensors has been well known, however, very little insight has been given on the effects of flow on EIS spectra. To our knowledge, we report for the first time that under high flow rates a second time constant can be observed.

2. Experimental

2.1 Lab-on-PCB design and fabrication

The Lab-on-PCB device was designed in a standard PCB design CAD software (Altium Designer®), comprising two layers: a gold-plated sensing electrode layer, housing the sensing electrodes, and a microfluidic layer including the sample delivery microfluidic channels (Fig. 1a). The sensing layer consists of two planar, circular electrodes and two cylindrical electrodes, used simultaneously as the fluidic inlet and outlet. Each PCB (Fig. 1b) houses 4 identical sensing electrode channels, for experimental practicality and sensor repeatability studies. All electrodes

are terminated in a PCI express edge connector interface (Fig. 1b-d), allowing effortless slot-type electrical connection of the device to the external instrumentation. For Electrochemical Impedance Spectroscopy (EIS) measurements a three-electrode configuration was employed (Fig. 1b).

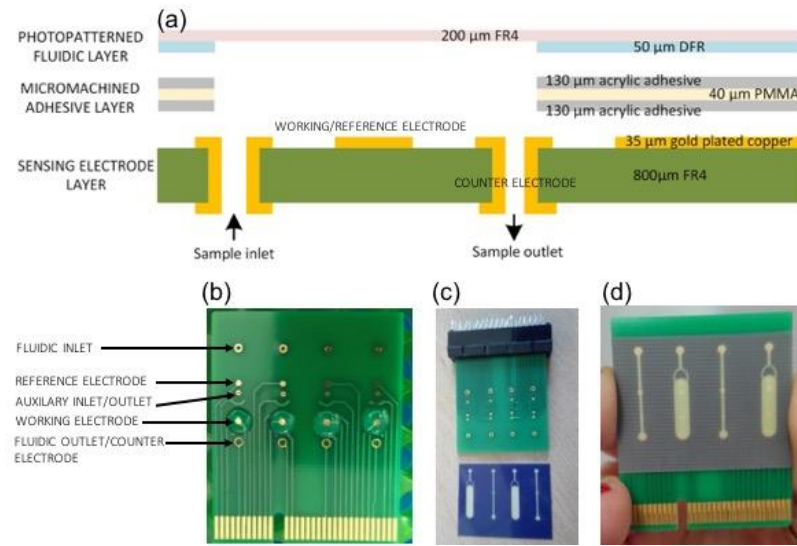


Figure 1. The exploited Lab-on-PCB biosensing platform: (a) Integrated Lab-on-PCB stackup; (b) Electrochemical Impedance Spectroscopy electrode configuration; (c) Commercially fabricated PCB biosensing platform; and (d) sample delivery microfluidics.

Two different commercial gold electroplating processes were evaluated: soft and hard gold plating. For the soft gold, the METALOR[®] MetGold Pure ATF process (Inc) was followed, providing a 2.57 μm thick gold layer of 90 HV hardness. For the hard gold, the METALOR[®] ENGOLDT[™] 2015CVR (Inc) process was followed, providing 2.41 μm gold on top of 3.41 μm Ni, with a final hardness of 140-180 HV.

For continuous flow experiments, the fluidic layer was adhered on top of the sensing layer to form the complete Lab-on-PCB platform. The main fluidic layer comprises a thin FR4 layer (to allow for the fluidic optical inspection), laminated with a 40 μm thick photo patternable dry film

photoresist (DFR). The resist is patterned via conventional photolithography and developed in a mild, basic solution of 1% sodium carbonate. The developed fluidic structure is subsequently post-baked for approximately 2 hours to assure DFR solvent evaporation. A custom adhesive layer was employed to form the final stack, laminating a 50 μm thick PMMA film with 3M 468MP acrylic adhesive; the adhesive layer was laser micromachined following the fluidic layer pattern and then pressed at room temperature between the fluidic layer and sensing layer to achieve leak-tight sample flow. Each Lab-on-PCB platform features two types of microfluidic channels (Fig. 1d): one with the minimum achievable width following our fabrication process (150 μm) and one with a much larger width (5 mm). While more narrow channels enable a smoother reagent flow, they often suffer from clogging, thus reducing the yield of flow-through devices. To this end, the wider channel design was incorporated on the same Lab-on-PCB platform, allowing the performance of flow experiments when the narrow channels were clogged. In order to minimize air bubble accumulation in the corners, a double inlet design is employed.

2.2 Physical and chemical characterization

The electrode surface roughness was evaluated via Atomic Force Microscopy (AFM) using a Digital Instruments Nanoscope IIIA and subsequent image analysis on the Nanoscope Analysis 1.5 software package. The chemical composition of the electrode surface was characterized using X-ray Photoelectron Spectroscopy (XPS). The spectra were recorded on a Thermo Scientific K-Alpha+ XPS system operating at 2×10^{-9} mbar base pressure. This system incorporates a monochromated, microfocused Al K α X-ray source ($h\nu = 1486.6$ eV) and a 180° double-focusing hemispherical analyzer with a 2D detector. The X-ray source was operated at 6 mA emission current and 12 kV anode bias, and a flood gun was used to minimize sample charging. Data were

collected at 200 eV pass energy for survey and 20 eV pass energy for core level and valence band spectra using an X-ray spot size of 400 μm . All data were analyzed using the Advantage software package.

Electrochemical impedance spectroscopy was performed using a three-electrode configuration with gold as counter and pseudo-reference electrode at equilibrium potential; impedance was measured between working and counter electrode exposed in 0.01 M PB (pH 7.4) measurement buffer containing 4 mM of ferro/ferricyanide $[\text{Fe}(\text{CN})_6]^{3-/4-}$ redox couple (hexacyanoferrate II/III). A 10 mV amplitude a.c. voltage in the frequency range of 100 kHz - 100 mHz was applied, without any external biasing, using a $\mu\text{Autolab III}$ / FRA2 potentiostat / galvanostat (Metrohm, The Netherlands). The cyclic voltammograms were also performed in a three-electrode configuration with the redox couple, cycling the potential between -0.4 V and 0.4 V (scan rate: 0.1 Vsec^{-1}). Open circuit potential measurements were recorded between two of the sensing electrodes (gold working and pseudo-reference electrode) exposed in the aforementioned measurement buffer.

For the continuous flow experiments, the reagents were delivered via a syringe pump (Cole Palmer 230-CE) into the Lab-on-PCB inlet. Interfacing fluidic tightness was achieved via a custom-made PMMA chip holder, housing Upchurch[®] polymer microfluidic ports and ferrules.

2.3 Biosensing assay and reagents

The gold plated electrodes were cleaned prior to probe immobilization by 10 min immersion in base piranha solution (5:1:1, water : ammonium hydroxide (20%) : hydrogen peroxide (30%)) followed by 5 min sonication in a sequence of acetone, propan-2-ol, and DI water. Clean gold electrodes were then co-immobilized with a thiolated single-stranded PNA (ssPNA) probe sequence and 6-mercapto-1-hexanol (MCH, Sigma-Aldrich, UK) in 50% dimethyl sulfoxide

(DMSO, Sigma-Aldrich, UK), 50% ultra-pure water (v/v). The immobilization solution was incubated on the working electrodes overnight in a humidity chamber at 4 °C. For the optimization studies, different ratios of PNA to MCH were studied in order to find the most efficient ratio for binding studies. A PNA probe having the sequence HS-(CH₂)₆-AEEEA-ACA-ACA-ACA-ACA-ACA (N- to C-terminus, where AEEEA is a 9-amino-4,7-dioxanonanoic acid linker) was suspended in a 1:1 volumetric ratio of DMSO:DI water to create a 100 µM stock. This stock was heated to 55 °C for 10 min in a dry block heater followed by vortex (30 s) then ultrasonication (1 min) before diluting to 1 µM aliquots in DMSO:DI (1:1, vol). After immobilization, the electrodes were rinsed with ultrapure water and dried with cleanroom grade air flow to remove any unattached thiols. In order to ensure complete thiol coverage of the gold surface, the electrodes were backfilled with 1 mM MCH in 0.01 M PB (pH 7.4) for 50 min. The electrodes were then rinsed with ultrapure water and placed in the measurement buffer (0.01 M PB, pH 7.4) for 1 hour to stabilize the self-assembled monolayer (SAM). The functionalized electrodes were then used to detect the target oligos. Different concentrations of the complementary TCT-TCT-TCT-TCT-TCT target single-stranded DNA (ssDNA) sequence in 0.01 M PB (pH 7.4) was used to prepare the calibration curve and complete mismatch CAC-CAC-CAC-CAC-CAC ssDNA sequences were used as a control. HPLC purified synthetic oligonucleotides were purchased from Sigma-Aldrich, UK in lyophilized form, while PNA probe sequences were purchased from Cambridge Research Biochemical, UK

3. Results and Discussion

In the first instance, the gold-plated sensing electrode layer (Fig. 1d) was exploited without the microfluidic layer attached, in order to characterize their electroactive behavior, identify any necessary surface pre-treatment steps, and optimize the detection assay.

3.1 Characterization of electrode electroplating processes.

Identical PCB electrodes, electroplated following both the soft and hard gold plating processes, were physically and chemically characterized, appreciating the significant impact that electrode surface roughness and chemical composition have on electrochemical biosensor performance (Salvo et al., 2014).

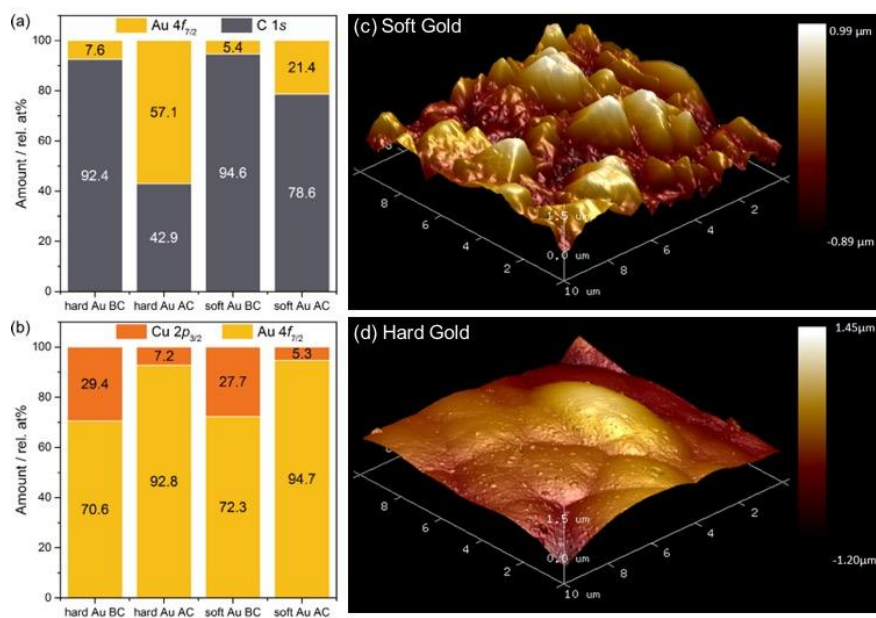


Figure 2. Surface characteristics of the soft and hard gold electrode surfaces before (BC) and after (AC) cleaning. (a) and (b): comparative plots of the Au:C and Au:Cu ratios derived from XPS measurements. The legends give the specific core level areas used for quantification. (c) and (d): AFM 3D representations of soft and hard gold.

AFM images for both electrode surfaces (Fig. 2c-d) revealed much more pronounced surface roughness for the soft gold process (soft gold: $R_{RMS}=413$ nm; hard gold: $R_{RMS}=266$ nm). Electrochemical characterization via cyclic voltammetry (CV) in the presence of $[\text{Fe}(\text{CN})_6]^{3-/4-}$ revealed that pristine electrode surfaces in both cases were not as electroactive as expected (see

Supplementary Material, Fig. S1), thus implying the presence of an overlying organic layer covering the gold area. Hence, the electrodes were cleaned prior to probe immobilization. After the cleaning step in the base piranha solution, the anticipated oxidation and reduction peaks were observed in both cyclic voltammograms with a peak to peak difference found to be around 80 mV. However, in the two plated electrodes, a different electroactive behavior was found, with mismatched peak heights. The soft gold demonstrated lower peak current (1.8 μ A) whereas, hard gold showed higher peak current (2.25 μ A).

To gain further insight into the surface chemistry of the electrodes made by the two commercial electroplating processes, XPS analysis was employed both before and after the base piranha cleaning process. Survey spectra of the samples show strong differences in the background shape before and after cleaning for both soft and hard Au (see Supplementary Material, Fig. S2). Whilst C, O, and Cu sit on relatively flat backgrounds, the Au core levels, including e.g. Au 4*f* and 4*d*, exhibit steep background line shapes. This is consistent with a surface structure where the Au electrode surface is buried under an organic overlayer of C and O, which also contains some Cu (Tougaard, 1996). In addition, the survey spectra also show small contributions from Si, Cl, N, and Na before cleaning, stemming from the commercial electroplating processes. Fig. 2a,b show the relative atomic ratios of Au:C and Au:Cu derived from fits of the peak areas of the core levels (shown in Supplementary Material, Fig. S3). For both soft and hard Au a clear reduction of both Cu and C is found after cleaning, however, the reduction in the organic overlayer is much more pronounced on the hard Au. On the soft Au C is only reduced by 17%, whilst it is reduced by 54% on the hard Au. Cu is greatly reduced by between 76 and 81% in both cases, giving relative Au purities (compared to Cu) of 94.7% and 92.8% for soft and hard Au, respectively. In particular,

1 more than three-fold greater efficiency of the organic overlayer removal makes the hard Au a
2 promising electrode surface.

3 4 *3.2 Optimization of PNA surface coverage*

5 The sensor fabrication was monitored step by step using cyclic voltammetry in 0.01 M PB (pH
6 7.4) measurement buffer containing 4 mM of ferro/ferricyanide $[\text{Fe}(\text{CN})_6]^{3-/4-}$ redox couple
7 (hexacyanoferrate II/III). As shown in Fig. 3d, a clean bare electrode gave a high peak current of
8 $2.25\ \mu\text{A}$ (black curve) which decreased to $1.8\ \mu\text{A}$ corresponding to a 20% decrease after incubation
9 overnight with PNA/MCH immobilization solution (blue curve). Such an observation could be
10 attributed to the modification of the surface with a biolayer comprising of PNA and MCH
11 representing a physical barrier to the redox couple. Furthermore, when the electrode was incubated
12 with 1 nM of target DNA (Fig. 3c), a further decrease in the current to $1.10\ \mu\text{A}$ corresponding to
13 a 36% change, was observed due to hybridization of PNA to DNA (Fig. 3d, red curve). Such a
14 molecular binding event leads to an increase in the negative charge on the electrode surface
15 providing further resistance to the redox couple. Based on the insights into the physical and
16 chemical characteristics of the sensing electrode, the PNA/DNA biosensing assay was
17 implemented (Fig. 3a-c).

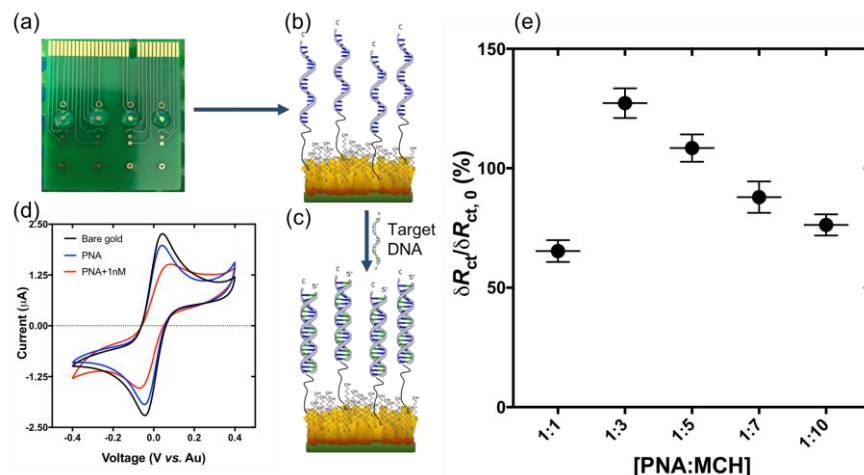


Figure 3. EIS biosensor assay optimization results: (a) Bare sensing electrodes, (b) schematic of co-immobilized PNA with MCH on sensing electrodes, (c) capture of target oligo (DNA), and (d) respective cyclic voltammograms in $[\text{Fe}(\text{CN})_6]^{3-/4-}$ following each assay step. (e) Charge transfer resistance difference $\Delta R_{ct}/R_{ct,0}$ recorded upon binding of 10 pM complementary DNA targets against PNA/MCH immobilization concentration ratios.

The surface density of probes plays a vital role in fabricating an efficient biosensor as reported with different techniques (Jolly et al., 2016; Keighley et al., 2008). An optimum spacing between the PNA probes on the surface is required to ensure minimum steric hindrance upon target DNA capture. Therefore, to maximize the biosensor impedance response, the PNA/MCH concentration ratio was optimized by recording the impedance spectra after the capture of 10 pM complementary DNA oligos for 5 different ratios and plotting the extracted charge transfer resistance $\Delta R_{ct}/R_{ct,0}$ against them (Fig. 3e). The graph shows a significant jump from 1:1 to 1:3 PNA/MCH ratio. Such an effect could be due to increased spacing between the PNA probes for easy recognition of sequence by the target DNA. As the ratios were increased from 1:3 to 1:10, a decrease in signal was observed. Such a decrease could be due to the formation of a diffuse layer by the MCH

resulting in the easy migration of redox couple to the electrode surface. Nevertheless, since the maximum $\Delta R_{ct}/R_{ct,0}$ was obtained for the 1:3 PNA/MCH ratio, and hence it was selected for the following biosensor characterization steps.

3.3 Analytical Performance

PNA probes were immobilized on pre-cleaned soft and hard PCB electrodes. The electrochemical impedance spectra were recorded upon capture of seven different concentrations of complementary DNA oligo, ranging from 100 fM to 100 nM (Fig. 4). The Nyquist plots obtained were fitted with the Randles equivalent circuit, with a constant phase element (non-ideal capacitance), in parallel with the charge transfer resistance (R_{ct}) and a Warburg element that models diffusion. The percentage-wise increase in charge transfer resistance, ($\Delta R_{ct}/R_{ct,0}$), is plotted against the logarithm of the target concentration in Fig. 4. As anticipated, an increase of $\Delta R_{ct}/R_{ct,0}$ with increasing concentration was observed for both PCB surfaces.

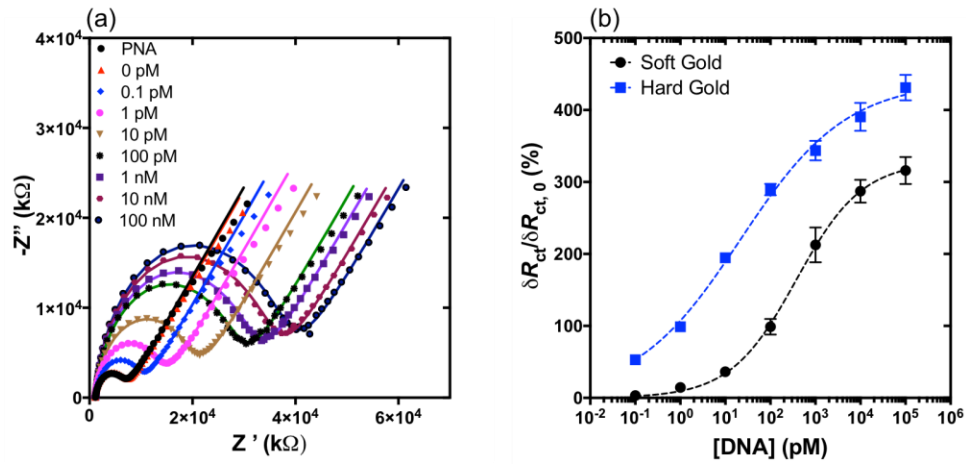


Figure 4. EIS PNA-DNA biosensor performance: (a) Typical Cole-Cole plots obtained with PNA PCB sensor for seven different DNA oligo concentrations and blank samples. (b) Charge transfer resistance difference $\Delta R_{ct}/R_{ct,0}$ calibration curve versus DNA target oligo concentration for both soft and hard electrode platings.

1 The typical Nyquist plots obtained using modified soft gold electrodes are presented in the
2 Supplementary Material (Fig. S4). Comparatively, hard gold electrodes result in much larger value
3 increases for the same target concentration, while at the same time demonstrating a much larger
4 linear range. The limit of detection for the hard gold surface sensors was calculated to be:
5 $LOD=3\sigma/slope=57$ fM, while for soft gold the limit is 307 fM. This difference in performance can
6 be ascribed both to the almost halved surface roughness of hard gold electrodes, resulting in better
7 SAM formation, as well as to the much more efficient gold cleaning highlighted in section 3.1;
8 more probes could be loaded on the less contaminated hard gold surfaces and in more spatially
9 orientated freedom. Using EIS, an initial R_{ct} of $4093 \pm 306 \Omega$ was observed with soft gold
10 electrodes modified with an optimized ratio of PNA and MCH, whereas with functionalized hard
11 gold there can be seen an initial R_{ct} of $6306 \pm 475 \Omega$. There was a significant difference in the
12 analytical performance of the soft and hard gold electrodes. For example, when the fabricated
13 electrodes were incubated with the lowest concentration of target DNA used (i.e. 100 fM), a signal
14 change of $53.09 \pm 1.33\%$ was observed with hard gold which was nearly 18 times higher than the
15 signal change observed with the soft gold ($3.17 \pm 1.72\%$). The dose-response curves obtained were
16 fitted with a standard hill slope equation for specific binding following the equation:
17 $Y=B_{max}*X^h/(K_d^h + X^h)$, where, B_{max} is maximum binding obtained, X is the concentration of
18 target, K_d is the dissociation coefficient and h is Hill slope describing cooperativity. Using this
19 equation, the dose-response data was fitted. An R squared value of 0.99 was obtained for the dose-
20 response curves of both soft and hard gold. It is worth mentioning that a higher K_d value was
21 observed for soft gold which was calculated to be 376.9 pM, while for the hard gold there was a
22 more than 4-fold difference, calculated to be 21.63 pM. For both the fittings, the value of h was
23 found to be below 1 (0.59 for soft gold and 0.37 for hard gold), which is a characteristic of

negatively cooperative binding; once one target molecule is bound to the PNA probe its affinity for other DNA target decreases. Following these observations, hard gold electrodes were chosen as biosensing platforms for all subsequent experiments.

3.3 Selectivity Studies

The development of a reliable biosensor depends on various factors, including the resolution to differentiate between specific and non-specific binding. The selectivity of the fabricated sensor was investigated with various control experiments to confirm that the signals obtained with target DNA were due to the specific binding event. The specificity of the hard gold PCB PNA sensors (Fig. 8) was evaluated by comparing the charge transfer resistance difference obtained for the lowest complementary DNA target concentration against those obtained for a blank buffer sample, a complete mismatch DNA sample, two common plasma proteins (Prostate Specific Antigen (PSA) and Human Serum Albumin (HSA)), and human plasma. The sensor demonstrates excellent specificity against all potentially interfering molecules. For example, the signal change observed with a 100 nM mismatch sequence was approximately $6.26 \pm 3.84\%$, while with 10 ng/mL PSA gave a similar value of $5.93 \pm 1.26\%$. Furthermore, 10 ng/mL HSA demonstrated a signal change of $0.56 \pm 2.76\%$ and human plasma a signal change of $5.73 \pm 4.14\%$. These signals, when compared with the lowest concentration of target DNA ($53.09 \pm 5.33\%$), were 10 times lower, demonstrating a specific interaction.

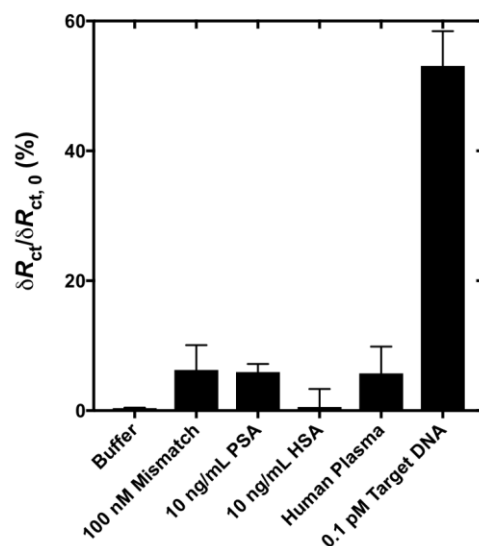


Figure 5. Charge transfer resistance difference $\Delta R_{ct}/R_{ct,0}$ values obtained against the blank sample, 100nM complete mismatch DNA oligo, 10 ng/mL Prostate Specific Antigen (PSA), 10 ng/mL Human Serum Albumin (HSA), and 0.1 pM complementary DNA oligo.

3.4 Integrated microfluidic system

Having characterized the electrochemical biosensors and identified the optimum electrode surface and biofunctionalization protocols, integration into a more compact Lab-on-PCB microsystem followed, including sample delivery microfluidics. The device was interfaced via a custom-made PMMA chip holder, housing commercially available fluidic ports and ferrules (Fig. 6a) to deliver the sample from the syringe into the microfluidic inlet and collect the waste from the outlet. The syringes were filled with complementary DNA samples and were serially injected into the Lab-on-PCB device via the microfluidics under a constant flow rate of 1 μ L/min. Each sample was injected continuously for 5 min (5 μ L volume) followed by a washing step of unbound molecules with buffer injection for another 5 min.

The EIS spectra of the sensors were then recorded in a three-electrode configuration, in order to compare the sensor behavior under continuous flow as opposed to the static experiments performed previously. The sensor was first tested with different flow rates ranging from no flow to 1 $\mu\text{L}/\text{min}$ and 100 $\mu\text{L}/\text{min}$ to challenge the sensor for drift analysis. The respective EIS spectra were recorded (Fig. 6b), showing negligible signal changes of $\sim 7\%$ with the tested flow rates, with a second semicircle appearing for the lower frequencies when the flow rate is increased to 100 $\mu\text{L}/\text{min}$. The intermediate flow rate (1 $\mu\text{L}/\text{min}$) was selected for the calibration of our sensor under flow, based on the R_{ct} calculation methodology used previously for the static experiments. The respective Nyquist plots for different complementary DNA concentrations are illustrated in Fig. S5 in the Supplementary Material, along with the extracted percentage-wise charge transfer resistance difference. A clear increase of $\Delta R_{\text{ct}}/R_{\text{ct},0}$ with increasing concentration is observed, however, the sensors seem to be reaching saturation at a lower concentration, compared to their static operation. This could be ascribed to more efficient molecule binding under continuous flow in a microfluidic channel of μL -scale volumes, minimizing molecule diffusion distances.

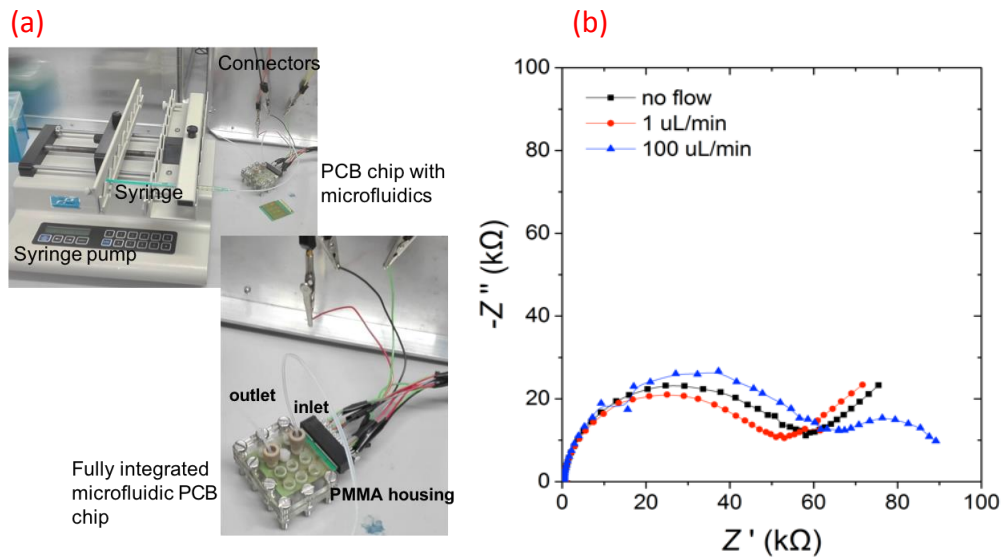


Figure 6. EIS biosensor characterization under continuous flow: (a) Lab-on-PCB PNA-based DNA quantification platform and experimental setup, integrating hard gold electrochemical sensors and sample-delivery microfluidics. (b) Nyquist plots obtained with different flow rates.

4. Conclusions

In this work a Lab-on-PCB DNA diagnostic platform was designed and fabricated, exploiting solely commercially available processing. The work systematically analyzes the importance of the microelectrode surface characteristics in achieving high sensitivities for PNA-based assays. Two alternative gold electroplating techniques were studied for their efficiency in electrochemical biosensing applications for the first time: soft and hard gold plating.

The PNA:MCH concentration ratio achieving the maximum charge transfer resistance $\Delta R_{ct}/R_{ct,0}$ increase upon binding of 10 pM complementary DNA targets was found to be 1:3. Following this optimized immobilization protocol, both hard and soft gold electrodes were biofunctionalized with PNA probes and the respective EIS analysis was performed across a range of 0.1 pM-105 pM target DNA, without employing the sample-delivery microfluidics. The $\Delta R_{ct}/R_{ct,0}$ calibration curves for the hard gold surfaces revealed the most sensitive results for PCB DNA electrochemical biosensors to date (LOD=57 fM, linear range: 100 fM-100 pM). This is ascribed to both the significantly smaller surface roughness ($R_{RMS}=266$ nm) as well as to the higher efficiency of organic overlayer removal during the electrode base piranha cleaning process, as confirmed by XPS analysis. The sensor also demonstrated excellent specificity against all studied interfering molecules (blank, 100 nM complete mismatch DNA oligo, 10 ng/mL PSA, 10 ng/mL HSA).

The PNA sensors were subsequently integrated with the commercially fabricated sample-delivery microfluidics, demonstrating the feasibility of high-sensitivity, cost-effective and rapid Lab-on-

1 PCB diagnostic microsystems. 5 μ L samples were analyzed in 5 minutes under continuous flow,
2 quantifying DNA samples within the range of 1 pM-100 pM. To our knowledge, we report for the
3 first time that under high flow rates a second time constant can be observed in the EIS spectra.
4 The current Lab-on-PCB platform shows saturation of the biosensors at much lower target DNA
5 concentrations under flow. Future work will focus on the optimization of sample flow rate and
6 sample volumes in order to achieve lower limits of detection, detailed investigation of the
7 mechanism behind the observed second time constant under increased flow rates, and further
8 integration of the presented platform with on-chip sample pretreatment microfluidics towards a
9 rapid and cost-effective, sample-in-answer out Lab-on-PCB diagnostic microsystem.

11 **Acknowledgements**

12 The authors wish to thank the Spirit Circuits Group and Lyncolec Ltd for their collaboration in
13 manufacturing the prototypes. AR acknowledges the support from Imperial College London for
14 her Imperial College Research Fellowship.

16 **References**

- 17 Abgrall, P., & Gué, A. M., 2007. Lab-on-chip technologies: making a microfluidic network and
18 coupling it into a complete microsystem. *Journal of Micromechanics and Microengineering*,
19 17(5), R15.
- 20 Aracil, C., Perdigones, F., Moreno, J. M., Luque, A., & Quero, J. M., 2015. Portable Lab-on-
21 PCB platform for autonomous micromixing. *Microelectronic Engineering*, 131, 13-18.
- 22 Bizzotto D., Burgess I. J., Doneux T., Sagara T., & Yu H.-Z., 2018, Beyond Simple Cartoons:
23 Challenges in Characterizing Electrochemical Biosensor Interfaces, *ACS Sens.* 2018, 3, 5–12.

1 Cai, B., Wang, S., Huang, L., Ning, Y., Zhang, Z., & Zhang, G.-J., 2014. Ultrasensitive label-
2 free detection of PNA–DNA hybridization by reduced graphene oxide field-effect transistor
3 biosensor. *ACS Nano*, 8(3), 2632-2638.

4 Chin, C. D., Linder, V., & Sia, S. K., 2012. Commercialization of microfluidic point-of-care
5 diagnostic devices. *Lab Chip*, 12(12), 2118-2134.

6 Fu, Y., Yuan, Q., & Guo, J., 2017. Lab-on-PCB-based micro-cytometer for circulating tumor
7 cells detection and enumeration. *Microfluidics and Nanofluidics*, 21(2), 20. doi:10.1007/s10404-
8 017-1854-2

9 Hintermüller, M. A., Jakoby, B., & Reichel, E. K., 2017. Numerical and experimental analysis of
10 an acoustic micropump utilizing a flexible printed circuit board as an actuator. *Sensors and*
11 *Actuators, A: Physical*, 260, 220-227. doi:10.1016/j.sna.2017.03.029

12 Hyrup, B., & Nielsen, P. E., 1996. Peptide nucleic acids (PNA): synthesis, properties and
13 potential applications. *Bioorganic & medicinal chemistry*, 4(1), 5-23.

14 Jolly, P., Batistuti, M. R., Miodek, A., Zhurauski, P., Mulato, M., Lindsay, M. A., & Estrela, P.,
15 2016. Highly sensitive dual mode electrochemical platform for microRNA detection. *Scientific*
16 *Reports*, 6, 36719. doi:10.1038/srep36719

17 Jung, W., Han, J., Choi, J.-W., & Ahn, C. H., 2015. Point-of-care testing (POCT) diagnostic
18 systems using microfluidic lab-on-a-chip technologies. *Microelectronic Engineering*, 132, 46-57.

19 Keighley, S.D., Estrela, P., Li, P., Migliorato, P., 2008. Optimization of label-free DNA
20 detection with electrochemical impedance spectroscopy using PNA probes. *Biosensors and*
21 *Bioelectronics* 24(4), 906-911

22 Mahato, K., Srivastava, A., Chandra, P., 2017. Paper based diagnostics for personalized health
23 care: Emerging technologies and commercial aspects. *Biosensors and Bioelectronics*, 96, 246-259.
24 doi:http://dx.doi.org/10.1016/j.bios.2017.05.001

25 Moschou, D., Greathead, L., Pantelidis, P., Kelleher, P., Morgan, H., & Prodromakis, T., 2016.
26 Amperometric IFN- γ immunosensors with commercially fabricated PCB sensing electrodes.
27 *Biosensors and Bioelectronics*, 86, 805-810. doi:http://dx.doi.org/10.1016/j.bios.2016.07.075

1 Moschou, D., & Tserepi, A., 2017. The lab-on-PCB approach: tackling the μ TAS commercial
2 upscaling bottleneck. *Lab on a Chip*, 17(8), 1388-1405.

3 Nilghaz, A., Guan, L., Tan, W., Shen, W., 2016. Advances of Paper-Based Microfluidics for
4 Diagnostics—The Original Motivation and Current Status. *ACS sensors*, 1(12), 1382-1393. doi:
5 10.1021/acssensors.6b00578

6 Salvo, P., Henry, O. Y., Dhaenens, K., Acero Sanchez, J. L., Gielen, A., Werne Solnestam, B.,
7 Vanfleteren, J., 2014. Fabrication and functionalization of PCB gold electrodes suitable for
8 DNA-based electrochemical sensing. *Biomed Mater Eng*, 24(4), 1705-1714. doi:10.3233/BME-
9 140982

10 Sanchez, J. L., Henry, O. Y., Joda, H., Solnestam, B. W., Kvastad, L., Johansson, E., O'Sullivan,
11 C. K., 2016. Multiplex PCB-based electrochemical detection of cancer biomarkers using MLPA-
12 barcode approach. *Biosens Bioelectron*, 82, 224-232. doi:10.1016/j.bios.2016.04.018

13 Tougaard, S., 1996. Surface nanostructure determination by x-ray photoemission spectroscopy
14 peak shape analysis. *Journal of Vacuum Science & Technology A: Vacuum, Surfaces, and*
15 *Films*, 14(3), 1415-1423.

16 van den Berg, A., & Lammerink, T. S., 1998. Micro total analysis systems: microfluidic aspects,
17 integration concept and applications. In *Microsystem technology in chemistry and life science*
18 (pp. 21-49): Springer.

19 Yetisen, A. K., Akram, M. S., & Lowe, C. R., 2013. based microfluidic point-of-care diagnostic
20 devices. *Lab Chip*, 13(12), 2210-2251.